Applied Physics Letters

Observation of localized acoustic skyrmions

Cite as: Appl. Phys. Lett. **122**, 022201 (2023); https://doi.org/10.1063/5.0131777
Submitted: 24 October 2022 • Accepted: 23 December 2022 • Published Online: 09 January 2023

Ping Hu, Hong-Wei Wu, Wen-Jun Sun, et al.

AIP Publishing

Applied Physics Letters ARTICLE scitation.org/journal/apl

Observation of localized acoustic skyrmions

Cite as: Appl. Phys. Lett. **122**, 022201 (2023); doi: 10.1063/5.0131777
Submitted: 24 October 2022 · Accepted: 23 December 2022 ·
Published Online: 9 January 2023

Ping Hu,[1] Hong-Wei Wu,[1,2,a)] Wen-Jun Sun,[1] Nong Zhou,[1] Xue Chen,[1] Yong-Qiang Yang,[1] and Zong-Qiang Sheng[1]

AFFILIATIONS

[1]School of Mechanics and Photoelectric Physics, Anhui University of Science and Technology, Huainan 232001, China
[2]National Laboratory of Solid State Microstructures, Nanjing University, Nanjing 210093, China

[a)]Author to whom correspondence should be addressed: hwwu@aust.edu.cn

ABSTRACT

Recently, acoustic skyrmions have been explored by tailoring velocity vectorial near-field distributions based on the interference of multiple spoof surface acoustic waves, providing new dimensions for advanced sound information processing, transport, and data storage. Here, we theoretically investigate and experimentally demonstrate that a deep-subwavelength spiral metastructure can also generate the acoustic skyrmion configuration. Analyzing the resonant response of the metastructure and observing the spatial profile of the velocity field, we find that the localized skyrmionic modes correspond to eigenmodes of the spiral structure. Thus, the skyrmionic modes do not require carefully tailored external excitation condition and they have multiple resonating frequencies unlike the single skyrmionic mode realized by the interference of multiple waves. We also demonstrate that the topological protected skyrmions supported by the subwavelength metastructure is robust against structure deformations and existence of structure defects. The real-space acoustic skyrmion topology may open new avenues for designing ultra-compact and robust acoustic devices, such as acoustic sensors, acoustic tweezers, and acoustic antennas.

Skyrmions are topologically protected quasiparticles, which was first proposed in nuclear physics by the British physicist Skyrme in 1962 to describe the interactions of pions.[1] Since then, the concept of skyrmions, the topological stability of the vectorial field configuration characterized by a topological integer number (called skyrmion number), has been considered in many subjects, such as nucleons,[2] Bose–Einstein condensates,[3,4] liquid crystals,[5,6] and magnetic materials.[7–10] Particularly, in magnetic materials, skyrmion has grown into a large research field and sprout various derivatives according to different topological textures beyond the elementary skyrmion, such as Néel type, Bloch type, anti-type, and higher-order Néel-type, even nested multiple skyrmions such as skyrmionium, bimeron, and bimeronium[11–17] Rich and varied textures of skyrmion modes offer large tunable degrees of freedom for promising applications in advanced information processing, high-density data storage, and transfer.[18,19] Light as an important information carrier has an urgent need for manipulating the vectorial textures of magnetic and electric fields. For this purpose, by constructing the evanescent electromagnetic field distribution in the especially shaped surface-plasmonic polariton structure,[20–22] the skyrmionics topological protected quasiparticle properties are emulated by the three-dimensional electric vector structure first in optical waves. Subsequently, various vectorial fields are constructed to realize optical skyrmions for offering new dimension to manipulate light-information processing, such as electric and magnetic vectors,[23] spin,[20,24,25] and synthesized pseudospin vectors.[26] Very recently, a familiar subwavelength space-coiling metastructure, which intrinsically supports the localized spoof plasmon skyrmionic modes, is also proposed to build arbitrarily shaped skyrmionic textures with multifrequency bands.[27,28]

It is well known that electromagnetic waves are vectorial field and logically construct the optical skyrmions. However, acoustic waves have long been recognized as spinless scalar waves. Until recently, this traditional view is updated, and the acoustic spin defined by the rotation of local velocity vector is observed in the interference of two acoustic waves propagating perpendicularly in free space or in the evanescent field of a guide mode traveling along a metamaterial waveguide.[29–33] The proposal of acoustic spin concept gives the opportunity to discuss the acoustic skyrmions. In this context, a hexagonal acoustic metasurface is designed to trap surface acoustic waves and form skyrmion lattice patterns for the dynamic acoustic velocity fields.[34] The topological robustness of the acoustic skyrmion lattice against disorders also be practical demonstrated by using the acoustic velocity sensing technique. However, based on the surface wave interference approach, the acoustic skyrmions not only have stringent requirement for external excitation conditions and lattice structure symmetry but also have the limitations of single-mode skyrmions at a given frequency.

In this work, we theoretically investigate and experimentally demonstrate the acoustic skyrmions configuration by using an Archimedes spiral structure with a subwavelength scale. Analyzing the resonant response of the metastructure and observing the spatial profile of the velocity field, we can observe the skyrmionic modes formed by the acoustic velocity field on the surface of the structure corresponding to the radial multi-orders resonant eigenmodes of the spiral structure. Unlike the interference-based approach, the skyrmions can be roused by both near field and far field. Furthermore, we also demonstrate that the topological protected skyrmions supported by the subwavelength metastructure is robust against structure deformations and existence of structure defects. The robust vectorial field topologies are preserved for the structure is continuously deformed in arbitrary shapes to build arbitrarily shaped skyrmionic textures. The real-space acoustic skyrmion topology may open new avenues for designing ultra-compact and advanced acoustic vectorial devices to manipulating of acoustic waves with flexible and robust acoustic structures.

We implement the acoustic skyrmionic modes using a spiral structure based on an Archimedean spiral line shape, the schematic diagram of the structure is shown in Fig. 1(a). The Archimedean spiral can be expressed in polar coordinates as $\rho(\theta)$, θ is the helix angle, and ρ is the radius of the helix at that angle. The total angle of the spiral winding is $2\pi n$ and the radius changes from r to $r + nd$. Therefore, the polar equation of the Archimedean spiral can be expressed as $\rho(\theta) = r + b\theta$ and $b = \frac{d}{2\pi}$ is the spiral growth rate. The structure details are as follows: gap width $a = 1.45\,mm$, spiral pitch $d = 2.45\,mm$, outer radius $R = 50\,mm$ and inner radius $r = 1\,mm$, wall thickness of $1\,mm$, height $h = 50\,mm$, and spiral rotation number $n = (R - r)/d$. We can calculate the total length of the Archimedean spiral by the formula for the arc length of the curve in polar coordinates: $L = \int_0^{2n\pi} \sqrt{\rho^2(\theta) + (\frac{d\rho}{d\theta})^2}\, d\theta = \int_0^{2n\pi} \sqrt{(r + b\theta)^2 + b^2}\, d\theta$; using the designed structural parameters, the total length can be obtained as $L = 3205.19$ mm.

For starter, Fig. 1(b) shows the pressure and velocity distributions supported on the well-designed spiral structure for the lowest order skyrmionic mode $m = 1$, where the order number m describes the flipped number of velocity vectors along the radial direction. The colors in the structure mark the pressure field distributions, while the color vectors above the structure represent the configuration of the velocity fields. It can be seen from the vector orientation that the velocity field vector is directed upward at the center $\rho = 0$ (ρ marks the radial direction coordinate), while with the increase in the radius, the direction of the velocity field gradually flips and is finally directed downward at a structure edge. In order to insight the origin of skyrmions, we investigate the resonance response of the spiral structure in a two-dimensional case for an incident plane acoustic wave. In this model, the spiral structure is equivalent to a half-truncated waveguide with one end closed and one end opened, using the formula for the arc length of the curve in polar coordinates, we can get the effective waveguide length as $l = 3079.94\,mm$. For the half-truncated waveguide, the Fabry–Pérot (FP) resonating condition gives that $\frac{\lambda_m}{2} + (m-1)\lambda_m = 2l$, where $m = 1, 2, 3, \ldots$. Therefore, the resonant wavelength of the $m-th$ order mode is $\lambda_m = \frac{4l}{2m-1}$. We depict the

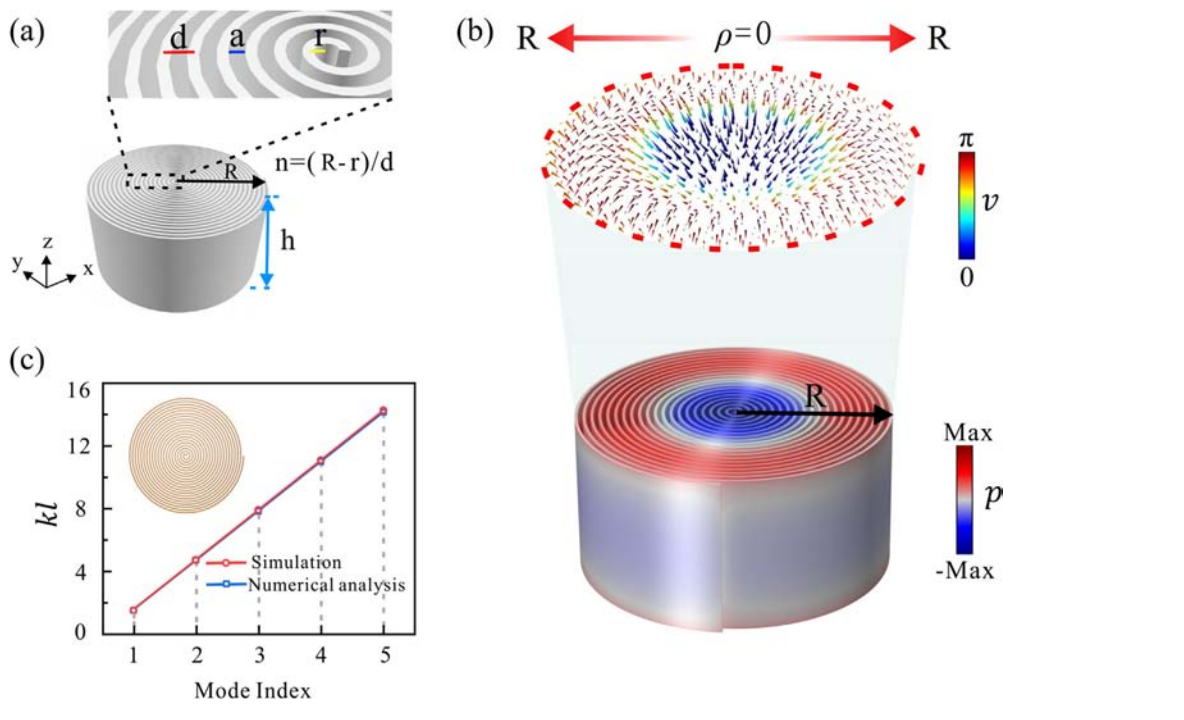

FIG. 1. Schematic structure and simulation results of the skyrmionic mode formed by the acoustic velocity field. (a) Schematic diagram of the structure, where R and r are the outer and inner radii, respectively, d is the spiral pitch, a is the gap width, n is the number of turns, and h is the structure height. (b) Simulation diagram of the skyrmionic mode formed by the acoustic velocity field, the direction of the acoustic velocity field is shown by the conical arrow in (c) Theoretical calculations and simulations of resonant responses in two-dimensional structures.

resonance modes in the two-dimensional case in Fig. 1(c), where the normalized variable $kl = 2\pi l/\lambda_m$ as a function of mode index m. We can see that the nearly isometric resonant modes, whose resonating frequency predicted by the FP resonating condition agrees well with the simulation results, can be seen that its resonant frequency is only determined by the effective waveguide length and mode number.

As mentioned earlier, we have given a demo for the lowest order skyrmionic mode and discuss the formation mechanism of resonating modes. Next, we will discuss the multi-order skyrmionic modes supported by the designed structure and their topological property. Figures 2(a)–2(c) show their acoustic velocity field distributions of the first-, second-, and third-order modes corresponded to resonating frequencies of 2720, 2981, and 3112 Hz at the surface of the structure [as shown in Fig. 1(a)]. Topological property of skyrmion modes is an important feature different to the trivial localized resonating modes in acoustic labyrinthic structures.[35,36] The topological property can be described by skyrmion number S, which be expressed by

$$S = \frac{1}{4\pi}\int\int dxdy\vec{n}\cdot(\partial_x\vec{n}\times\partial_y\vec{n}). \tag{1}$$

In our model, the velocity field distributions $\vec{v}$ can define the acoustic skyrmion number according to Eq. (1), where $\vec{n} = Re(\vec{v})/|Re(\vec{v})|$. The velocity field vectors can be represented as the distribution unwrapped from a sphere parametrized by longitude α and latitude β, which are the functions of the velocity along the radial flip angle φ and the radius ρ, respectively. The corresponding schematic diagram is shown in Figs. 2(a)–2(c). Thus, the skyrmion number can be expressed by the following equation:

$$S = \left(\frac{1}{2}\int_0^R \sin\beta(\rho)d\rho\right)\left(\frac{1}{2\pi}\int_0^{2\pi}\frac{d\alpha(\varphi)}{d\varphi}d\varphi\right). \tag{2}$$

Then, the skyrmionic number can divide into the polarity part $P = \frac{1}{2}\left[\cos\beta(\rho)\right]\big|_{\rho=0}^{\rho=R}$, vorticity part $M = \frac{1}{2\pi}[\alpha(\varphi)]\big|_{\varphi=0}^{\varphi=2\pi}$, and $\alpha(\varphi) = m\varphi$ for Néel-type skyrmionic modes. Figures 2(d)–2(f) show the schematic diagram of the velocity field distributions of the first three modes and their corresponding radial sound pressure field distribution. We can find that the velocity field direction flipped times are 1, 2, and 3 for the first three skyrmionic modes along the radial direction. According to Eq. (2), it can be concluded that the total number of skyrmion corresponding to odd twists of the velocity field along the radial direction is $S = 1$ and even twists is $S = 0$ as shown in Figs. 2(g)–2(i).

It is well known that the skyrmionic modes are topologically protected against the structure deformation and existence of structure defects. Here, we constructed an elliptical shape and a square shape, as shown in Figs. 3(a) and 3(b), respectively, and the two kinds of spiral structures can also maintain good stability when the geometry changes

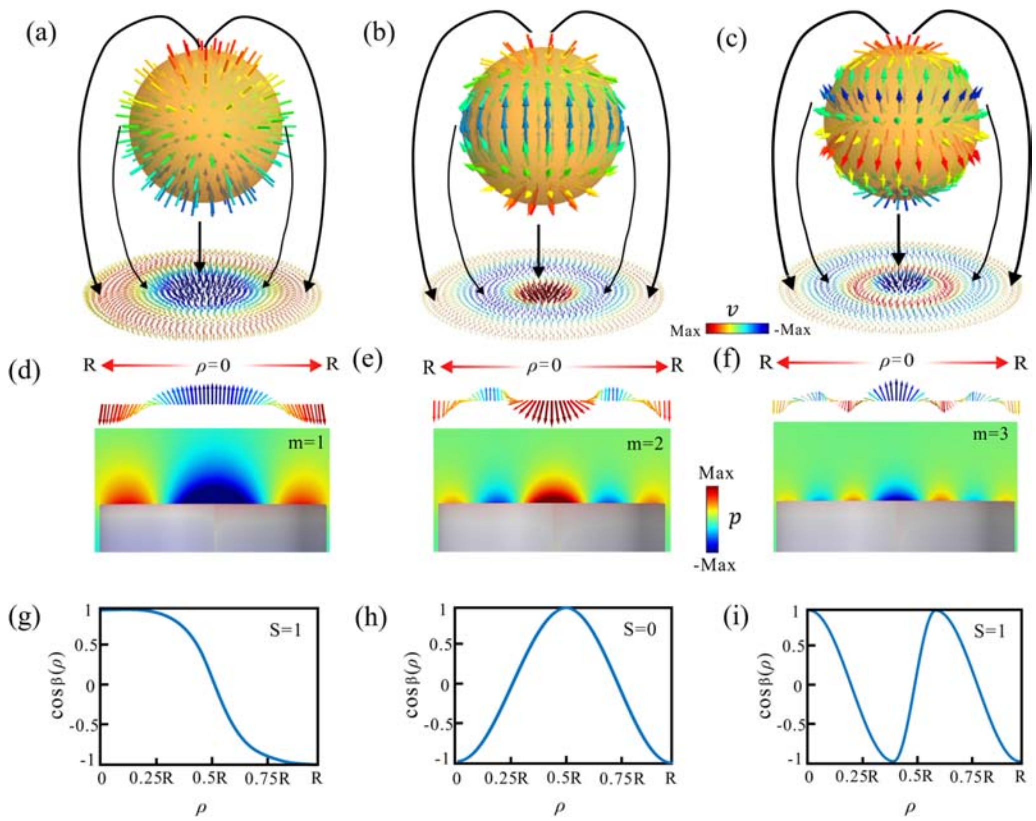

FIG. 2. Multiple order modes of skyrmion formed by acoustic velocity fields and skyrmionic numbers. (a)–(c) Acoustic velocity field distributions of the first-, second-, and the third-order modes, respectively. (d)–(f) Schematic diagram of the sound pressure field and the distribution of the sound velocity field in the cross section of the structure for corresponded modes. (g)–(i) The total skyrmion number of related modes along the radial direction are $S = 1$, $S = 0$, $S = 1$.

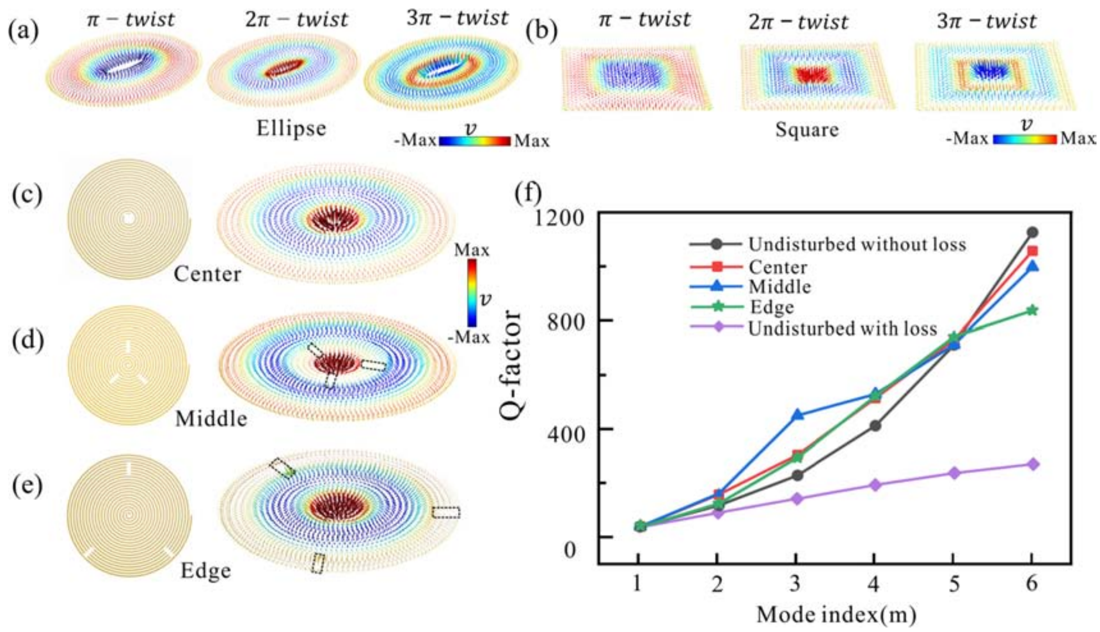

FIG. 3. Skyrmionic modes of spiral structures with deformation/defects and their topological properties. (a) and (b) Skyrmionic modes generate on the surface of the oval and square spiral structures. (c)–(e) The second-order skyrmionic modes for the cavity-type defects are at the center, middle, and edge of the structure, respectively. (f) The Q factor of the first six skyrmionic modes with/without defects and with/without losses.

and can also form skyrmionic modes and does not affect its velocity field vector distribution. Furthermore, to verify the robustness of the skyrmionic mode of the acoustic velocity field, we place defects at the center, middle position, and edge of the structure in different directions by tailoring cavity-type defects, as shown in the schematic diagram of the structure in Figs. 3(c)–3(e), where the defects disrupt the continuity of the slits in the structure. From the simulation results in Figs. 3(c)–3(e), the defects have less effect on the skyrmionium modes, only a small perturbation in the acoustic velocity field near the defects, and the overall skyrmionium mode is still very obvious, indicating that the structure is robust to the perturbation of the defects. A structure with height h = 50 mm and R = 50 mm is selected for the main study, and we also calculate the structure for different heights and radii. When the radius (or height) of the structure is constant, its eigenfrequency decreases with the increase in height (or radius) (see the supplementary material for details). An important application of skyrmion is the storage of information. The quality factor (Q factor) as an important physical quantity to evaluate the performance of the storage devices; thus, we also calculated the Q factor of this spiral structure at different orders with and without defects as shown in Fig. 3(f), respectively. The Q factor[37,38] is calculated as $Q = \mathrm{Re}(\omega)/[-2\mathrm{Im}(\omega)]$. We can find that the Q factor increase with the increase in the mode index. Particularly, the Q factors of the structure with defects are consistent with the value of the perfect structure. In order to better understand the structural properties, we have studied the influence of thermal viscosity. The topological protection properties allow the formation of a skyrmionic-like mode, but the quality factor is much lower compared to the normal mode due to the high losses as shown in Fig. 3(f).

To observe the acoustic skyrmion phenomenon in the experiment, we first implemented the acoustic skyrmionic modes using the simulation software COMSOL Multiphysics with a pressure acoustic module, as shown in Figs. 4(b) and 4(c). Under the pressure acoustic frequency domain module, we place a point source at a distance of 10 cm from the edge of the structure along the x-axis direction and excite the first- and the second-order skyrmionic modes at 2720 and 2980 Hz, respectively. We fabricated the sample using 3D printing according to the structure in the simulation, as shown in the inset of Fig. 4(d), we generated a sine wave signal with incident frequency $f = 2720\,Hz$ by a signal generator (AFG1022, Tektronix) and then amplified it with a power amplifier (CPA2400, SinoCinetech) to drive a loudspeaker and excite the experimental sample along the x-axis direction, then measured its sound pressure distribution along the diameter on the sample surface, as shown in the blue area of Fig. 4(d). Meanwhile, we also give the sound pressure magnitude and distribution of the simulation results along the diameter, as shown in the red area in Fig. 4(d), the reason for the cylindrical distribution of the sound pressure field is that the pressure field mainly distribute in the slit of the structure. The measured and simulated sound pressure distributions of the sample at 2980 Hz are shown in Fig. 4(f). Then, we can obtain the magnitude and direction of the corresponded sound velocity fields using measured sound pressure field distribution by $\vec{v} = \frac{1}{i\omega\rho_0}\nabla p$ (here, ω and ρ_0 are the angular frequency and mass density of air). The simulated and experimental results of sound velocity field distribution along the blue dashed line of sample [inset of Fig. 4(d)] are shown in Figs. 4(e) and 4(g) for the first- and second-order skyrmionic modes. We can find that the experimental result (blue arrows) agrees well with the simulated result (red arrows).

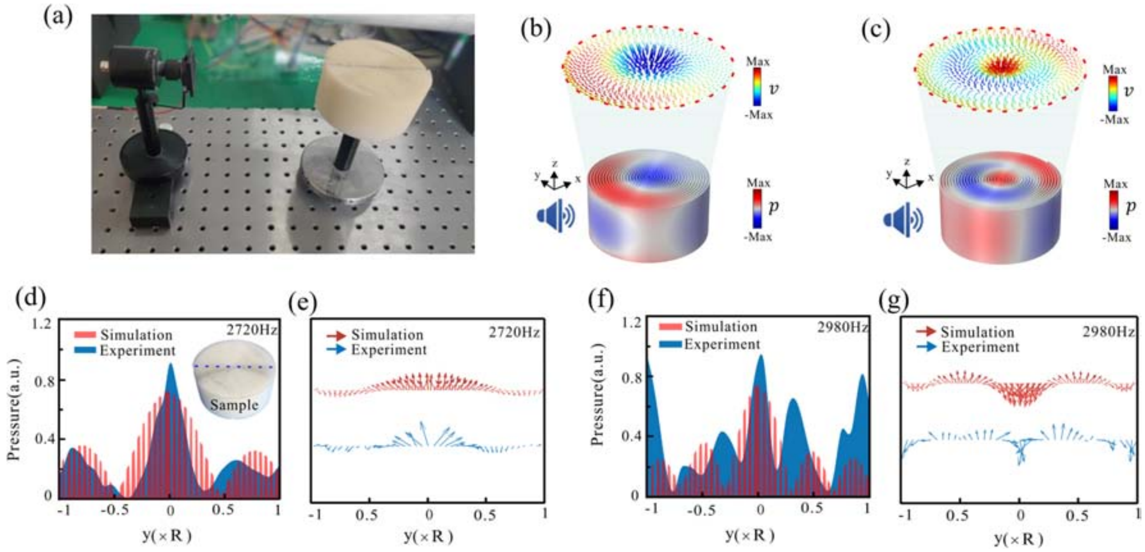

FIG. 4. Experimental measurement of the cross-sectional sound pressure field distributions and their sound velocity field distributions. (a) Photographs of the experimental setup. (b) and (c) The first- and second-order skyrmionic modes at frequency $f = 2720Hz$ and $f = 2980Hz$ in numerical simulation excited by a small acoustic source. (d) and (f) Simulated (red) and experimentally measured (blue) cross-sectional sound pressure field distribution along the blue dashed line on the surface of sample as shown as an inset for the first- and second-order skyrmionic modes. (e) and (g) Cross-sectional acoustic velocity field distributions for simulation (red arrows) and experiment (blue arrows) for the two skyrmionic modes, respectively.

In order to verify the stability of the structure under different deformations, we also performed frequency domain simulations and experimental measurement for the square structure. Figures 5(b), 5(d), and 5(e) describe the skyrmionic modes formed by the excitation of the square structure in the frequency domain, and the acoustic pressure field and velocity field distribution by the experimental measurement at 2770 Hz are agree well with the simulated results. Also, we implemented the skyrmionium mode at resonating frequency 3010 Hz, as shown in Figs. 5(c), 5(f), and 5(g). These experimental results indicate that the skyrmionic modes are robust to the deformation of the structure.

In this work, we use this Archimedean spiral structure to realize the localized acoustic skyrmionic modes by manipulating the acoustic

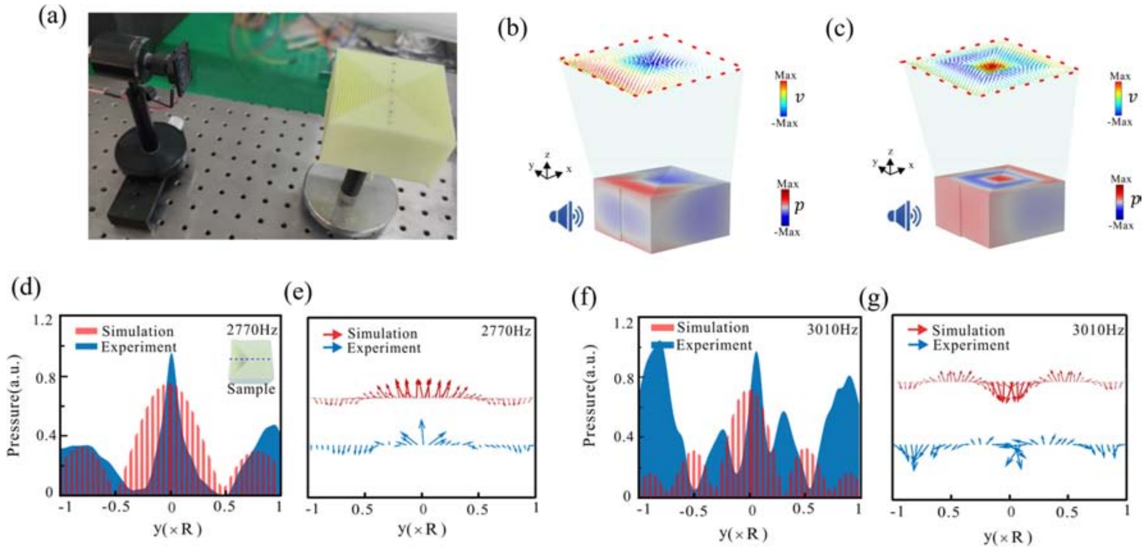

FIG. 5. Simulation and experimental results of the square structure. (a) Photographs of the experimental setup. (b) and (c) The first- and second-order skyrmionic modes at frequency $f = 2770Hz$ and $f = 3010Hz$ in numerical simulation excited by a small acoustic source. (d) and (f) Simulated (red) and experimentally measured (blue) cross-sectional sound pressure field distribution along the blue dashed line on the surface of sample as shown as an inset for the first- and second-order skyrmionic modes. (e) and (g) Cross-sectional acoustic velocity field distributions for simulation (red arrows) and experiment (blue arrows) for the two skyrmionic modes, respectively.

velocity field distributions. These localized skyrmion velocity fields profiles correspond to eigenmodes of the spiral structure. Thus, the skyrmionic modes do not require carefully tailored external excitation condition comparing with the interference-based approach of skyrmionic lattice. Furthermore, the subwavelength structure can support multiple skyrmionic eigenmodes with different frequencies unlike the single skyrmionic mode realized in phononic crystals. We also demonstrate that the topological protected skyrmions supported by the subwavelength metastructure is robust against structure deformations and existence of structure defects. These rich physical properties of acoustic localized skyrmionic modes offer the possibility of their future use in the control of tiny particles and the storage of acoustic information.

See the supplementary material for the influence of structure parameters on the skyrmionic modes.

This work was supported by the National Natural Science Foundation of China (NSFC) (Grant No. 11904008); the Natural Science Foundation of Anhui Province (Grant No. 1908085QA21), and the China Postdoctoral Science Foundation (Grant No. 2019M662132).

AUTHOR DECLARATIONS

Conflict of Interest

The authors have no conflicts to disclose.

Author Contributions

Ping Hu: Data curation (equal); Investigation (equal); Writing – original draft (equal). **Hong-Wei Wu:** Conceptualization (equal); Investigation (equal); Writing – original draft (equal); Writing – review & editing (equal). **Wen-Jun Sun:** Data curation (equal); Investigation (equal). **Nong Zhou:** Data curation (equal); Investigation (equal). **Xue Chen:** Supervision (equal). **Yong-Qiang Yang:** Supervision (equal). **Zong-Qiang Sheng:** Supervision (equal).

DATA AVAILABILITY

Data underlying the results presented in this paper are not publicly available at this time but may be obtained from the corresponding author upon reasonable request.

REFERENCES

[1] T. H. R. Skyrme, Nucl. Phys. **31**, 556 (1962).
[2] G. S. Adkins, C. R. Nappi, and E. Witi, Nucl. Phys. **228**, 552 (1983).
[3] U. Al Khawaja and H. Stoof, Nature **411**, 918 (2001).
[4] S. W. Su, I. K. Liu, Y. C. Tsai, W. M. Liu, and S. C. Gou, Phys. Rev. A **86**, 023601 (2012).
[5] J. I. Fukuda and S. Žumer, Nat. Commun. **2**, 246 (2011).
[6] A. Duzgun, J. V. Selinger, and A. Saxena, Phys. Rev. E **97**, 062706 (2018).
[7] U. K. Roessler, A. N. Bogdanov, and C. Pfleiderer, Nature **442**, 797 (2006).
[8] Y. Tokura and N. Kanazawa, Chem. Rev. **121**, 2857 (2021).
[9] S. Mühlbauer, B. Binz, F. Jonietz, C. Pfleiderer, A. Rosch, A. Neubauer, R. Georgii, and P. Böni, Science **323**, 915 (2009).
[10] X. Z. Yu, W. Koshibae, Y. Tokunaga, K. Shibata, Y. Taguchi, N. Nagaosa, and Y. Tokura, Nature **564**, 95 (2018).
[11] X. Zhang, J. Xia, Y. Zhou, D. Wang, X. Liu, W. Zhao, and M. Ezawa, Phys. Rev. B **94**, 094420 (2016).
[12] S. Zhang, F. Kronast, G. van der Laan, and T. Hesjedal, Nano Lett. **18**, 1057 (2018).
[13] M. M. M. Bhukta, A. Mishra, G. Pradhan, S. Mallick, B. B. Singh, and S. Bedanta, arXiv:1810.08262 (2018).
[14] I. Kezsmarki, S. Bordacs, P. Milde, E. Neuber, L. M. Eng, J. S. White, H. M. Rønnow, C. D. Dewhurst, M. Mochizuki, K. Yanai, H. Nakamura, D. Ehlers, V. Tsurkan, and A. Loidl, Nat. Mater. **14**, 1116 (2015).
[15] A. K. Nayak, V. Kumar, T. Ma, P. Werner, E. Pippel, R. Sahoo, F. Damay, U. K. Rößler, C. Felser, and S. S. P. Parkin, Nature **548**, 561 (2017).
[16] D. A. Gilbert, B. B. Maranville, A. L. Balk, B. J. Kirby, P. Fischer, D. T. Pierce, J. Unguris, J. A. Borchers, and K. Liu, Nat. Commun. **6**, 8462 (2015).
[17] J. Xia, X. Zhang, M. Ezawa, O. A. Tretiakov, Z. Hou, W. Wang, G. Zhao, X. Liu, H. T. Diep, and Y. Zhou, Appl. Phys. Lett. **117**, 012403 (2020).
[18] N. Nagaosa and Y. Tokura, Nat. Nanotechnol. **8**, 899 (2013).
[19] A. Fert, N. Reyren, and V. Cros, Nat. Rev. Mater. **2**, 17031 (2017).
[20] L. Du, A. Yang, A. V. Zayats, and X. Yuan, Nat. Phys. **15**, 650 (2019).
[21] T. J. Davis, D. Janoschka, P. Dreher, B. Frank, F. J. Meyer zu Heringdorf, and H. Giessen, Science **368**, eaba6415 (2020).
[22] S. Tsesses, E. Ostrovsky, K. Cohen, B. Gjonaj, N. H. Lindner, and G. Bartal, Science **361**, 993 (2018).
[23] C. Bai, J. Chen, Y. Zhang, D. Zhang, and Q. Zhan, Opt. Express **28**, 10320 (2020).
[24] K. Y. Bliokh, F. J. Rodríguez-Fortuño, F. Nori, and A. V. Zayats, Nat. Photonics **9**, 796 (2015).
[25] P. Shi, L. Du, and X. Yuan, Nanophotonics **9**, 4619 (2020).
[26] A. Karnieli, S. Tsesses, G. Bartal, and A. Arie, Nat. Commun. **12**, 1092 (2021).
[27] Z. L. Deng, T. Shi, A. Krasnok, X. Li, and A. Alù, Nat. Commun. **13**, 8 (2022).
[28] X. Li, L. Liu, Z. Zhou, J. Shen, Y. Zhang, G. Han, and Z. Li, Adv. Opt. Mater. **10**, 2200331 (2022).
[29] C. Shi, R. Zhao, Y. Long, S. Yang, Y. Wang, H. Chen, J. Ren, and X. Zhang, Natl. Sci. Rev. **6**, 707 (2019).
[30] L. Burns, L. Burns, K. Y. Bliokh, F. Nori, J. Dressel, and J. Dressel, New J. Phys. **22**, 053050 (2020).
[31] Y. Long, D. Zhang, C. Yang, J. Ge, H. Chen, and J. Ren, Nat. Commun. **11**, 4716 (2020).
[32] K. Y. Bliokh and F. Nori, Phys. Rev. B **99**, 020301 (2019).
[33] K. Y. Bliokh and F. Nori, Phys. Rev. B **99**, 174310 (2019).
[34] H. Ge, X. Y. Xu, L. Liu, R. Xu, Z. K. Lin, S. Y. Yu, M. Bao, J. H. Jiang, M. H. Lu, and Y. F. Chen, Phys. Rev. Lett. **127**, 144502 (2021).
[35] H. W. Wu, W. Li, S. L. Cheng, Y. Q. Yin, and Z. Q. Sheng, Appl. Phys. Express **14**, 095501 (2021).
[36] Y. Cheng, C. Zhou, B. G. Yuan, D. J. Wu, Q. Wei, and X. J. Liu, Nat. Mater. **14**, 1013 (2015).
[37] F. Monticone and A. Alu, Phys. Rev. Lett. **112**, 213903 (2014).
[38] H. W. Wu, Y. Fang, J. Q. Quan, Y. Z. Han, Y. Q. Yin, Y. Li, and Z. Q. Sheng, Phys. Rev. B **100**, 235443 (2019).